Inelastic Strain and Damage in Surface Instability Tests

Chu-Shu Kao[1] · Ali Tarokh[2] · Luigi Biolzi[3] · Joseph F. Labuz[2]

Received: 29 September 2014 / Accepted: 10 May 2015

1 Introduction

Failure of rock near a free surface such as a tunnel wall is often manifested as spalling or slabbing (Stacey 1981; Diederichs 2007; Andersson et al. 2009). Localized damage or fracture usually appears parallel to the free face, and the rock spalls or slabs from a linking of microcracks. Breakouts surrounding highly stressed boreholes are also related to surface spalling (Vardoulakis and Papanastasiou 1988; Ewy and Cook 1990). It is challenging for engineers to determine material parameters, which form the basis of a constitutive law, to predict the conditions for spalling to occur.

On the laboratory scale, the spalling mechanism under uniaxial compression has been studied throughout the post-peak phase. In a uniaxial compression test with end constraint eliminated, it has been observed that localized damage (fracture) forms parallel to the axial loading direction and is visible as axial splitting (Wawersik and Fairhurst 1970; Hudson et al. 1971; Peng and Johnson 1972). It has also been explained that if the specimen boundaries are not lubricated (Vardoulakis et al. 1998), the failure mode is often of a shear type accompanied by cone-shaped end zones.

The failure mechanism and processes of surface instability have been considered for several decades from the axial splitting phenomenon, typically in uniaxial compression tests. Nemat-Nasser and Horii (1982) studied compression-induced nonplanar crack extension (wing cracks) using a polymer resin. With a number of randomly oriented cracks of the same size, the failure pattern showed

✉ Ali Tarokh
tarok001@umn.edu

Joseph F. Labuz
jlabuz@umn.edu

[1] ExxonMobil Upstream Research Company, Houston, USA

[2] Department of Civil, Environmental, and Geo- Engineering, University of Minnesota, Minneapolis, USA

[3] Politecnico di Milano, Milan, Italy

that tension cracks initiated at tips of several pre-existing cracks, and extension occurred in the direction of maximum compressive stress. The linkage of cracks close to the free boundaries resulted in axial splitting. Horii and Nemat-Nesser (1985) extended the research by using multiple sizes of flaws to study splitting and faulting (shear failure). Under uniaxial loading, it was reported that the coalescence of cracks leads to axial splitting, even with a large array of preferential flaws spanning the specimen to promote faulting. Thus, the Griffith theory provided a premise that axial splitting starts from the nucleation of flaws, which may be an essential feature to all investiga-tions of brittle failure.

In this paper, the surface instability phenomenon was reproduced in laboratory tests with a specially designed apparatus and the failure processes of sandstones were observed by applying the acoustic emission (AE) and digital image correlation (DIC) techniques to monitor microcracking. AE and DIC are complimentary, in that AE samples the volume with location resolution of millimeters while DIC measures surface displacements with resolution of microns. A continuum damage mechanics model was implemented and the damage parameters were found.

2 Experimental Procedure

2.1 Design and Instrumentation

In laboratory experiments, the uniaxial compression test with lubricated ends exhibits axial splitting, a type of surface instability phenomenon, but due to the cylindrical shape of the specimen and the loss of symmetry when splitting begins, it is generally difficult to evaluate the state of strain quantitatively. The surface instability apparatus (SIA) was designed for simulating spalling behavior under plane-strain conditions (Fig. 1a), which is achieved by using a stiff frame so that the strain in one direction (z-direction) is below a tolerable value. The design of this device was inspired by the wedge-test apparatus used by Schäpermeier (1979) to perform rock bursting tests on coal. A prismatic specimen is placed on a lower platen and fully confined by two stiff side walls, secured with the aid of a wedge located on the left side wall. The use of the wedge allows a small pre-stress to be developed to ensure proper contact of the specimen with the stiff frame. The rock is compressed axially (y-direction) and the interme-diate stress is then generated passively due to the Poisson's effect of the specimen in the z-direction (Fig. 1b). This loading configuration promotes surface spalling at the free face. The front wall does not contact the specimen and guarantees a traction-free, exposed face, while the rear wall ensures lateral deformation and spalling at the front. A detailed description can be found in Papamichos et al.(1994).

An open window is machined in the front wall (Fig. 1a), providing space for lateral displacement measurements and mounting of acoustic emission (AE) transducers. The SIA is made of mild steel and the five walls—top, bottom, rear, and two side walls—contacting the specimen lined with a hardened Rockwell C55 polished steel platens (12.7 mm thick) to reduce friction. In order to capture images on the specimen surface, namely the σ_1–σ_3 (i.e., y–x) plane, while performing surface instability tests, the SIA was modified such that a digital camera can "see" the specimen surface through the side wall. In addition, the plane-strain condition should not be compromised as the specimen is stressed. The modification involved cutting a window of 50 × 63.5 mm in the steel sidewall (Fig. 1c). The size was selected to provide appropriate coverage of the image and maintain reasonable stiffness of the side wall. An annealed glass plate, manufactured from soda lime glass with float glass processes (Brin Glass Company, Minneapolis, MN, USA), replaced the original hardened steel platen lining between the specimen and the sidewall.

The SIA is placed within either a 1 MN or 3 MN load frame (MTS Systems Corporation, Eden Prairie, MN), depending on the rock type and load required to fail the specimen. Axial and lateral displacements are measured by linear variable differential transformers (LVDTs). The actuator mounted LVDT measures the axial displacement (stroke) that includes the displacement of the apparatus' parts and load frame along the loading axis. Correction of apparatus deformation is performed for each test. The lateral displacement of the specimen is measured by one LVDT with a linear range of ±1 mm, linearity of 0.15 %. The SIA has eight (8) pre-drilled holes in the sidewalls, four on each side, for installing pin-type, piezoelectric AE sensors that contact the specimen's surfaces; Fig. 1a shows two positions for the AE sensors and additional sensors can be mounted on the free face. AE activity generated upon loading the specimen are monitored by these piezoelectric transducers communicating with a high-speed data recorder.

2.2 Specimen Preparation

The specimen is a precisely machined, right orthogonal prism sized at 110 mm × 90 mm × 80 mm (length × height × width). Each face of the specimen was machined parallel to the opposite face and orthogonal to the adjacent ones. The parallelism of faces was ±10 μm. The accuracy on specimen dimensions has a larger tolerance of ±0.5 mm on the width of specimen, while the tolerance on height and length of the specimen is ±1 mm. The text matrix is shown in Table 1.

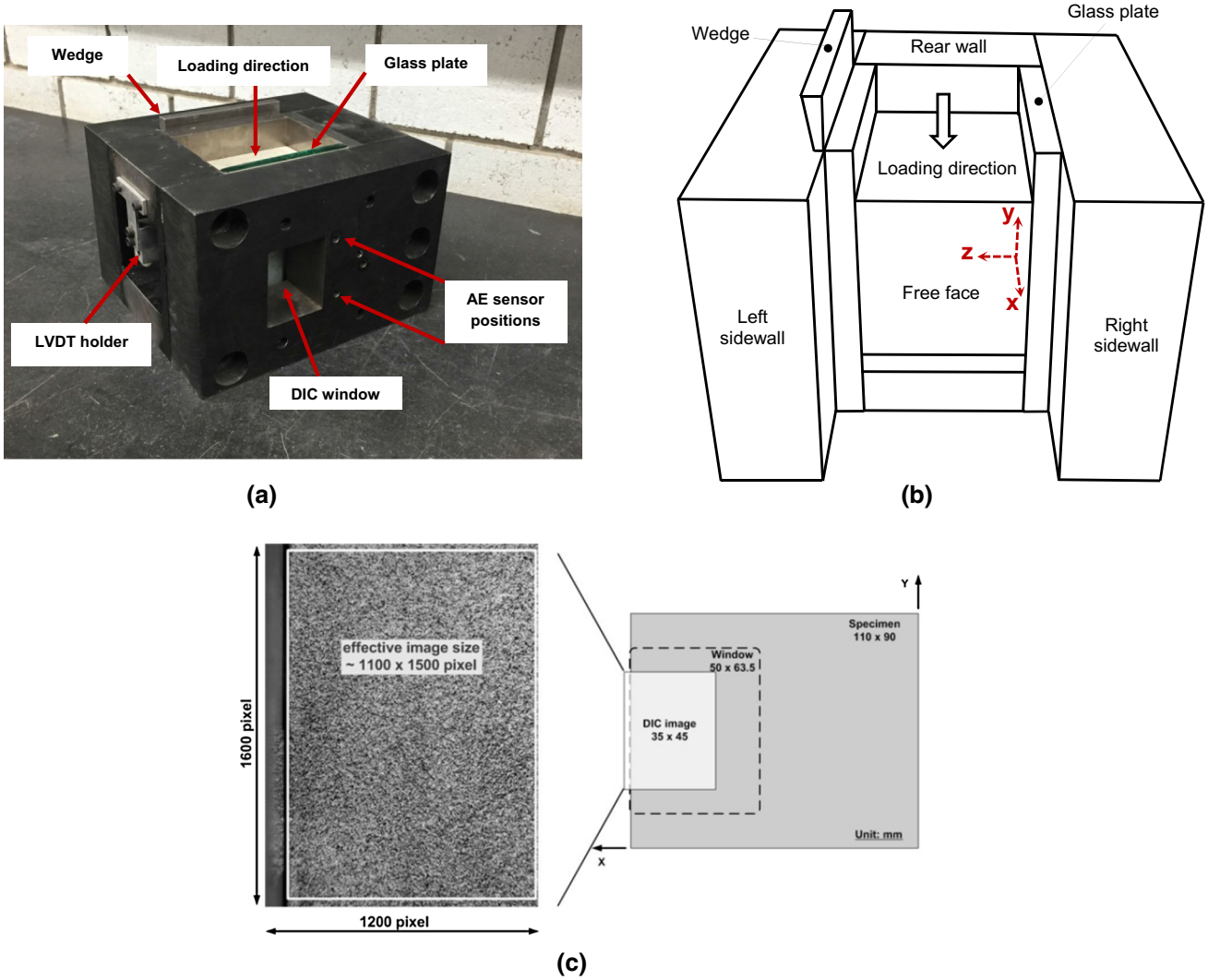

Fig. 1 Surface instability apparatus. **a** Photograph showing DIC window; **b** schematic view of the apparatus without front wall; **c** relative sizes of specimen, machined window, and DIC image at $z = 0$ mm. The origin of the coordinate system is located at the lower right corner of the specimen in contact with the rear wall

Table 1 Surface instability tests on two types of sandstones

Test number	Rock type	AE	DIC	Note
SISS05[a]	Serena sandstone	–	✔	Virgin material
SISS06[a]	Serena sandstone	–	✔	600 °C heated
SISS08[a]	Serena sandstone	–	✔	Virgin material
SIBS10	Berea sandstone	✔	✔	Virgin material
SIBS11	Berea sandstone	✔	✔	Virgin material
SIBS12	Berea sandstone	✔	✔	Virgin material

[a] Tested in 3 MN load frame

Berea and Serena sandstones were studied. Berea sandstone is obtained from Cuyahoga County in northeast Ohio. It has no visible macroscopic features and shows thin bedding. The rock is light gray, medium-to-fine grained with uniformly distributed grain size of 0.1–0.8 mm and a median size of 0.2 mm. The major mineral constituents are 78 % quartz and 16 % feldspar (Krech et al. 1974). The tested Berea sandstone has the following mechanical and physical properties: Young's modulus $E = 10$–14 GPa, Poisson's ratio $\nu = 0.25$–0.30, density $\rho = 2450$ kg/m^3, porosity $n = 20$–22 %, bending tensile strength $\sigma_t = 3.4$–3.6 MPa, and UCS $= 28$–32 MPa. The P-wave velocity $c_p = 2280 - 2320$ m/s perpendicular to bedding and 2410–2470 m/s parallel to bedding. Serena sandstone, obtained from a quarry in Firenzuola, Italy, is a grayish, fine-grained stone with average grain size of 0.1 mm, categorized as a feldspathic greywacke with a large amount of clay matrix and low calcite content. Mineral compositions are quartz (32 %), alkaline feldspar (7 %), calcite (13 %), plagioclases (13 %), dolomite (7 %),

phyllosilicates and other minerals (28 %) (Biolzi et al. 2011). The mechanical and physical properties for this rock are $E = 28$–30 GPa, $\rho = 2580$ kg/m^3, $n = 3$–4 %, UCS = 100–120 MPa, $c_p = 3600$ m/s. One specimen of the Serena sandstone was heated to 600 ° C to produce further initial damage in the rock, in contrast to the virgin material. Description of the thermal treatment can be found in Biolzi et al. (2011).

2.3 Testing Procedure

To achieve the desired boundary conditions, a friction reducer, stearic acid, was applied to the interface between the material and loading platens (Labuz and Bridell 1993). The lower loading platen of the SIA was centered on a steel base plate, and the lubricated specimen was placed on the lower loading platen of the SIA. As shown in Fig. 1a, the rear, front, and two side walls were brought together and hand-tightened with ten bolts, and then torqued to 200 Nm (150 lb ft); a wedge assembly provided a tight fit (Fig. 1b). One lateral LVDT was secured in place with an LVDT holder mounted on the front wall of the SIA, and the LVDT was adjusted to contact the centroid of the specimen's front face, where a 15 mm diameter brass tab was attached.

The surface instability tests were controlled by a closed-loop system (MTS Flextest60 controller) with in-house written procedures programmed in MTS Series 793 control software. Two steps of control were used: (1) the specimen was loaded up to approximately 30 % of the UCS using load control with a loading rate of 2 kN/s; (2) a dynamic mode switch to lateral LVDT control of 0.5×10^{-3} mm/s was implemented until the specimen failed. The lateral displacement corresponds to the monotonically increasing parameter associated with a surface instability phenomenon.

2.4 Data Analysis

Data were recorded at a frequency of 1 Hz, including axial (compressive) load measured by the load cell, axial displacement (stroke) measured by the actuator mounted LVDT, and lateral displacement. The axial displacement contains displacement of the loading machine, including the SIA, loading platens, and all the parts in the axial loading axis. The machine displacement contributes to a significant part of the axial displacement (Fig. 2), and a correction was applied to the axial displacement data. The results presented as axial stress (axial force/area), corrected axial strain (axial displacement/height), and average lateral strain (lateral displacement/length) of the sandstones are presented in Fig. 3. All the surface instability tests were terminated when a spalling phenomenon occurred abruptly (causing the system to lose control), or a steady growth of

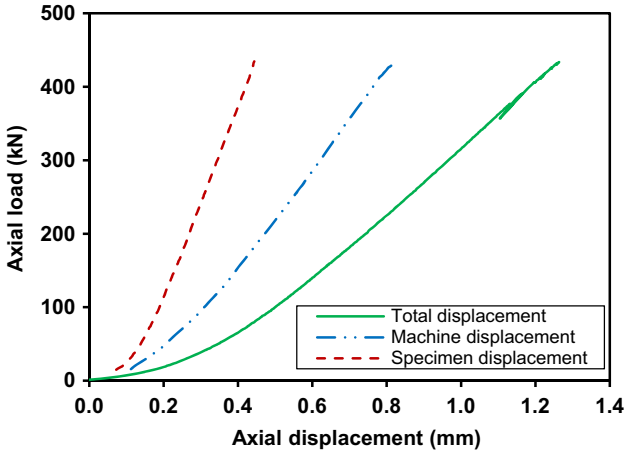

Fig. 2 Correction of machine displacement from stroke (axial displacement) to obtain specimen displacement

localized damage was observed without increasing axial load. Note the softer response of the heat-treated specimen (SS06).

3 Acoustic Emission

3.1 System Configuration

The AE system is composed of (1) an array of AE sensors; (2) signal conditioner and preamplifier; (3) signal digitizer; (4) a computer-based data acquisition system. A total of eight AE transducers were used, with two different models selected. The SIA equipped with eight pre-drilled holes in the sidewalls, which fit pin-type AE sensors (Dynasen piezoelectric pin CA-1136), having a diameter of 2.4 mm (0.093 in), height of 38.1 mm (1.5 in), frequency response of 0.2–2.0 MHz. These piezoelectric "pins" were secured by silicon glue. The stearic acid lubricant coated on the specimen also acted as a couplant for the pin-type AE sensors in the sidewalls. Another model of AE sensor (Physical Acoustics model S9225) was used on the exposed free face, secured using cyanoacrylate adhesive. The S9225 sensor has a frequency response from 0.3 to 1.8 MHz, diameter of 3.6 mm (0.15 in), height of 2.4 mm (0.1 in).

AE signals were preamplified (Physical Acoustics S1220C), with 40 dB gain and a 0.1–1.2 MHz band-pass filter. Typical noise level at the output of the preamplifiers was around ±2 mV. The waveforms were digitized and recorded by a high-speed DAQ system with four, two-channel modular transient recorders (National Instrument model NI-5112 digitizer) of 8-bit ADC resolution. The sampling rate was set at 20 MHz over a 200 μs window, with a 100-μs pretrigger. The recording system was triggered when the signal amplitude from a selected channel,

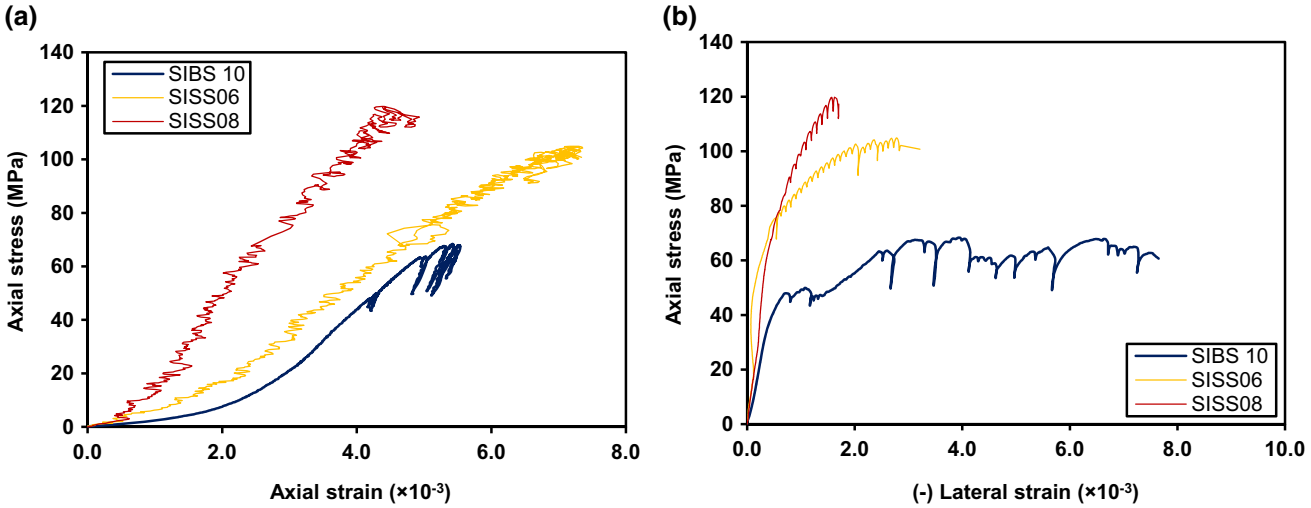

Fig. 3 Loading history for Berea and Serena sandstones in surface instability tests: **a** axial stress vs axial strain; **b** axial stress vs lateral strain. The heat-treated Serena sandstone (SISS06) clearly exhibits a different response compared to virgin Serena sandstone (SISS08)

the so-called "anchor" sensor, exceeded a preset threshold of ±30 mV. The whole process was controlled by an in-house program written in LabView, and the data recording was continuous.

3.2 AE Locations

The AE technique was employed on Berea sandstone specimens, with two AE sensors mounted on the front face and three sensors in each side wall. Acoustic activities at different loading stages for one of the Berea sandstone specimen (SIBS10) are presented in Fig. 4, where LR is the percentage of peak force. A total of 8050 events were recorded, with 1716 events successfully located. Before the peak load was reached, the AE location pattern was scattered, but locations were close to the free face ($x = 110$ mm). As the load approached peak, AE locations started to shift to a more confined region, but no local-ization was readily identified. In the post-peak stage, AE locations diffused into the interior part of the specimen.

4 Digital Image Correlation

4.1 Overview

Digital image correlation (DIC) is a particle-tracking method that uses digital images to generate displacement fields. The purpose of a particle-tracking technique is to retrieve a full-field measurement of displacement or velocity. This requires (a) an optical system to capture images; (b) a targeted object that locally features unique speckle patterns; and (c) an algorithm to construct the full-field measurement from pattern correlation (Lin and Labuz 2013). The digital particle-tracking technique is becoming popular in mechanics due to its powerful capability of evaluating full-field displacement. This makes determining the strain field feasible, which is impossible when using traditional types of transducers such as LVDTs or strain gages that only provide global displacement on the boundaries or average strain measurement within a small region.

4.2 Displacement Fields

Images from the specimen surface through the side wall were taken at a frequency of 1 Hz (1 frame/s) until the end of the surface instability tests. Typically more than a thousand frames were captured in each experiment. The selection of the images for processing was based on the LR. Special attention was given to frames close to peak load, with LR = 90, 95, 98, 99, 100 %.

4.2.1 Displacement Field at LR < 80 %

The incremental displacement fields are decomposed into x–y components called the vertical or axial component Δv (y-direction) and the horizontal or lateral component Δu (x-direction). As shown in Fig. 1c, the positions of the DIC images range from $x = 75$–110 mm, $y = 20$–65 mm, where $x = 110$ mm is the location of the free face. Fig-ure 5 shows the horizontal and vertical displacement con-tours plotted in the left and right columns at LR = 40–50, 50–60, 60–70, 70–80 %. Relative displacement vectors, meaning that the displacements at the inner-center point on the image ($x = 78$ mm, $y = 43$ mm) were taken as zero,

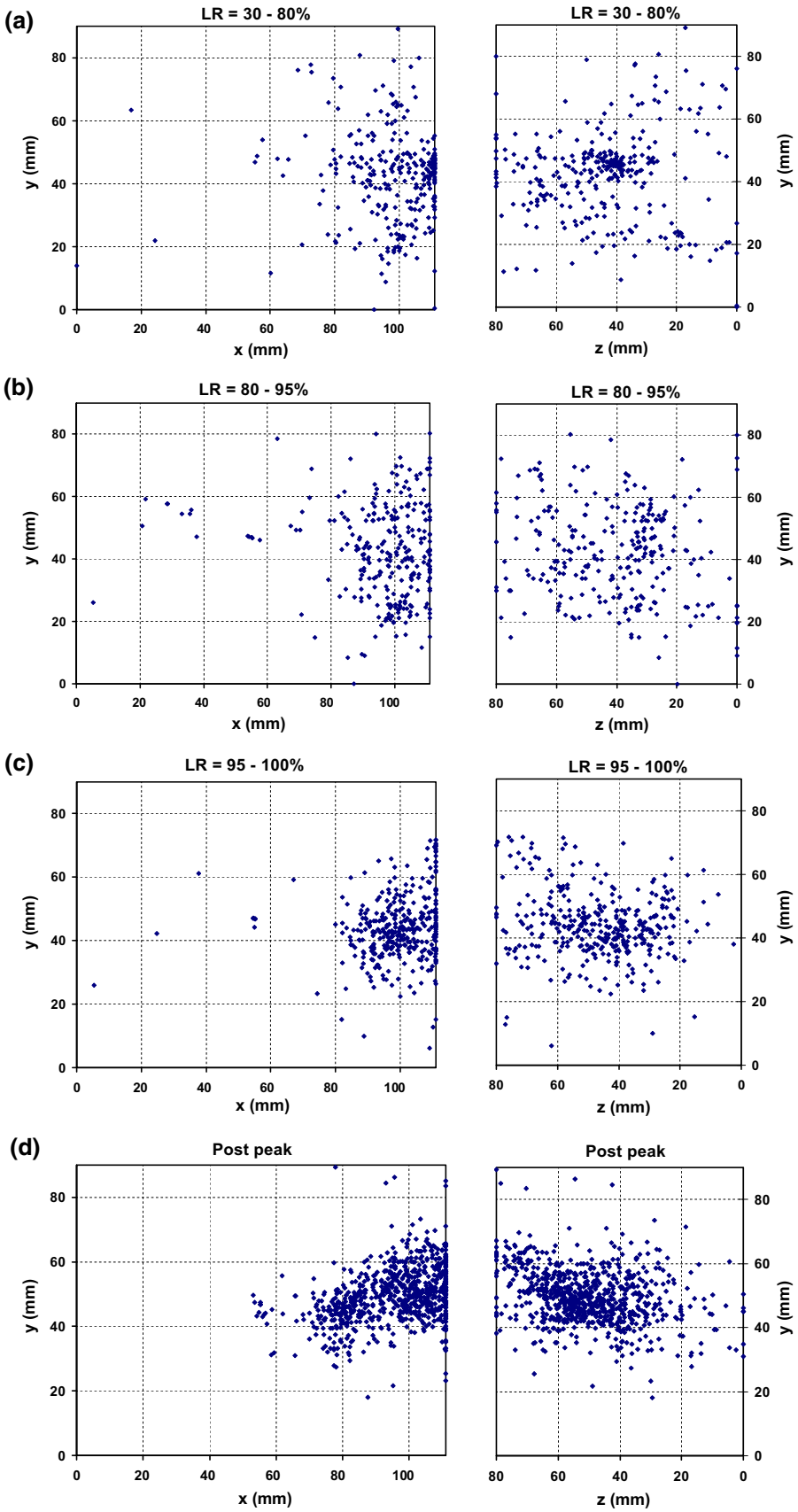

Fig. 4 AE locations of the surface instability test on Berea sandstone (SIBS10) at different loading stages:
a LR = 30–80 %;
b LR = 80–95 %;
c LR = 95–100 %; **d** post-peak stage

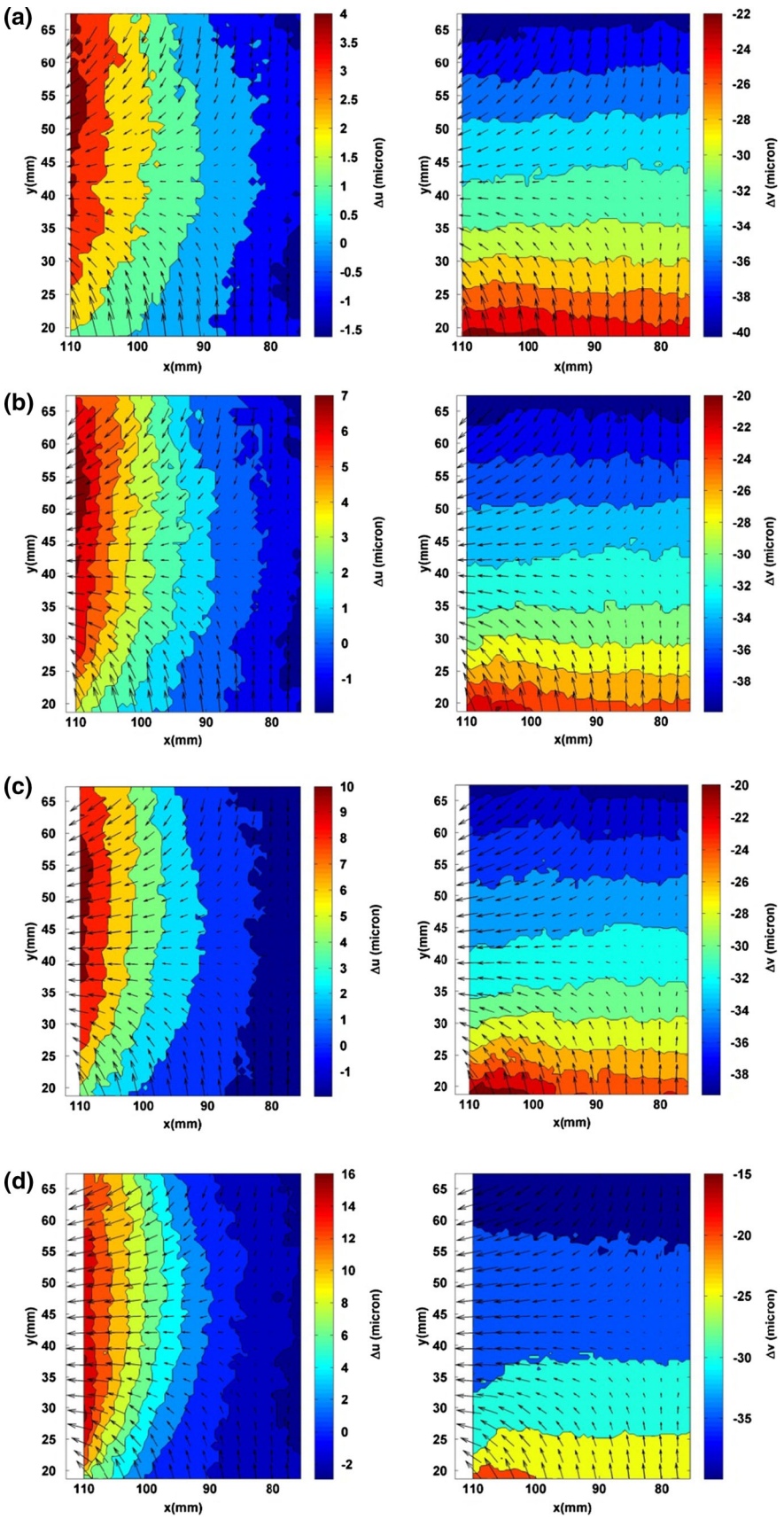

Fig. 5 Incremental horizontal (Δu) and vertical (Δv) displacement fields for test SIBS 10 at LR: **a** 40–50 %; **b** 50–60 %; **c** 60–70 %; **d** 70–80 %

are also presented. This zeroing enhances the free surface effects by removing the assumed homogeneous deformation of the interior. Note that positive displacements Δu and Δv follow the positive directions of the x–y coordinate system.

As shown in Fig. 5, the horizontal deformation has vertically or sub-vertically "striped" contours showing that the lateral displacement is uniformly distributed across the y-direction, and values are larger near the free face ($x = 110$ mm) while decreasing gradually at locations away from the free face. Similarly, the vertical deformation has horizontally striped contours showing that the axial displacement is uniformly distributed across the x-direction, and the values decrease from top to bottom of the image. These uniform fields do not change until 70–80 % LR. The vertical displacement contours show no obvious change but some "curving," while the lateral displacement field reveals a group of more closely spaced contour lines near the free face. This observation signifies that the free-face effect was becoming more significant. In addition, some boundary effects from the steel platens may influence the displacement field at higher levels of loading even though a lubricant was used to reduce end friction.

4.2.2 Displacement Field at 80 < LR < 100 %

The displacement field starts to distort at LR = 80–90 %, due to the accumulated damage near the free face and effects from the possible damage localization outside the field of view; the localized damage propagated into the field of view forming a spall before reaching peak stress. The incremental displacement fields at various LR from 80 to 100 % are presented in Fig. 6, where horizontal and vertical displacements are plotted in the left and right column. At 80–90 % LR (Fig. 6a), the incremental dis-placement field showed obvious change from Fig. 5a, visible from the "flow" of the vectors, which was due to damage starting to accumulate near the free face. At this level of LR, the displacement pattern near the free face ($x > 100$ mm) was associated with the lateral displacement being the predominant component. At $x > 100$ mm, the axial displacement was almost uniform for a zone from $y = 18$–67 mm. At the inner part of the specimen ($x < 100$ mm), the axial displacement field displayed a gradual transition along the y-direction pertaining to a constant gradient, similar to the observations at LR < 70 %. On the other hand, the lateral displacements increase significantly from $x = 95$ mm, while the inner part of the specimen deformed with a very low gradient in the x-direction. This band of high displacement gradient occurred at $x = 95$–105 mm at the mid-height of specimen ($y = 45$ mm), and curved towards the free face. The lateral displacement increased by more than 20 μm across this band, and then plateaued around $x = 105$ mm, 5 mm away from the free face.

At 90–95 % LR (Fig. 6b), a jump in displacement can be interpreted as localized damage starting from the bottom of the image at $x = 105$ mm, propagating upwards across the field of view. The localized damage was especially clear in the lateral displacement field, since fractures in a surface instability problem form parallel to the maximum compressive stress. The displacement vectors indicate that the spall displaced outward (positive x-direction) with relative expansion in the y-direction due to the axial unloading caused by the separation of the spall.

From 95 to 100 % LR (Fig. 6c–e), the surface spall displaced outwards in the lateral direction with a smaller downward component in the axial direction. At 95–98 %LR (Fig. 6c), the inner part of the specimen behaved as if it was at LR below 70 % with regard to the displacement field; the axial displacement contour showed horizontal stripes, meaning that fairly uniform compression occurred in the deeper region of the specimen, away from the free face.

Interestingly, at 98–100 % LR (Fig. 6d, e), a new region with localized damage occurred at $x = 100$ mm, $y = 18$–32 mm, creating a small segment next to the first spall, and it can be identified with different lateral (horizontal) and axial (vertical) displacements on the newly separated segment. The new segment moves away later-ally, but performs as if it "wedged" into the material from the bottom of the frame.

Here, only one test of Berea sandstone (SIBS10) is presented, but other tests including those of Serena sandstone reveal similar observations: the displacement field starts to distort at LR of 70–80 %, due to the accumulated damage near the free face and effects from the possible damage localization outside the field of view. Afterwards, the localized damage propagated into the field of view forming a spall before reaching the peak stress.

5 Damage Model for Surface Instability

5.1 Overview

Continuum damage modeling has been shown to be effective in describing the effects of distributed damage, which involves degradation of material stiffness and damage-induced anisotropy (Kachanov 1986, 1993; Krajcinovic 1983, 1989; Lemaitre 1985). A damage parameter can be defined to represent defects (e.g., microcracks) and their distribution. The damage parameter works as an internal variable, like strain and stress in classical elasticity, and its evolution may be specified by independent kinetic equations.

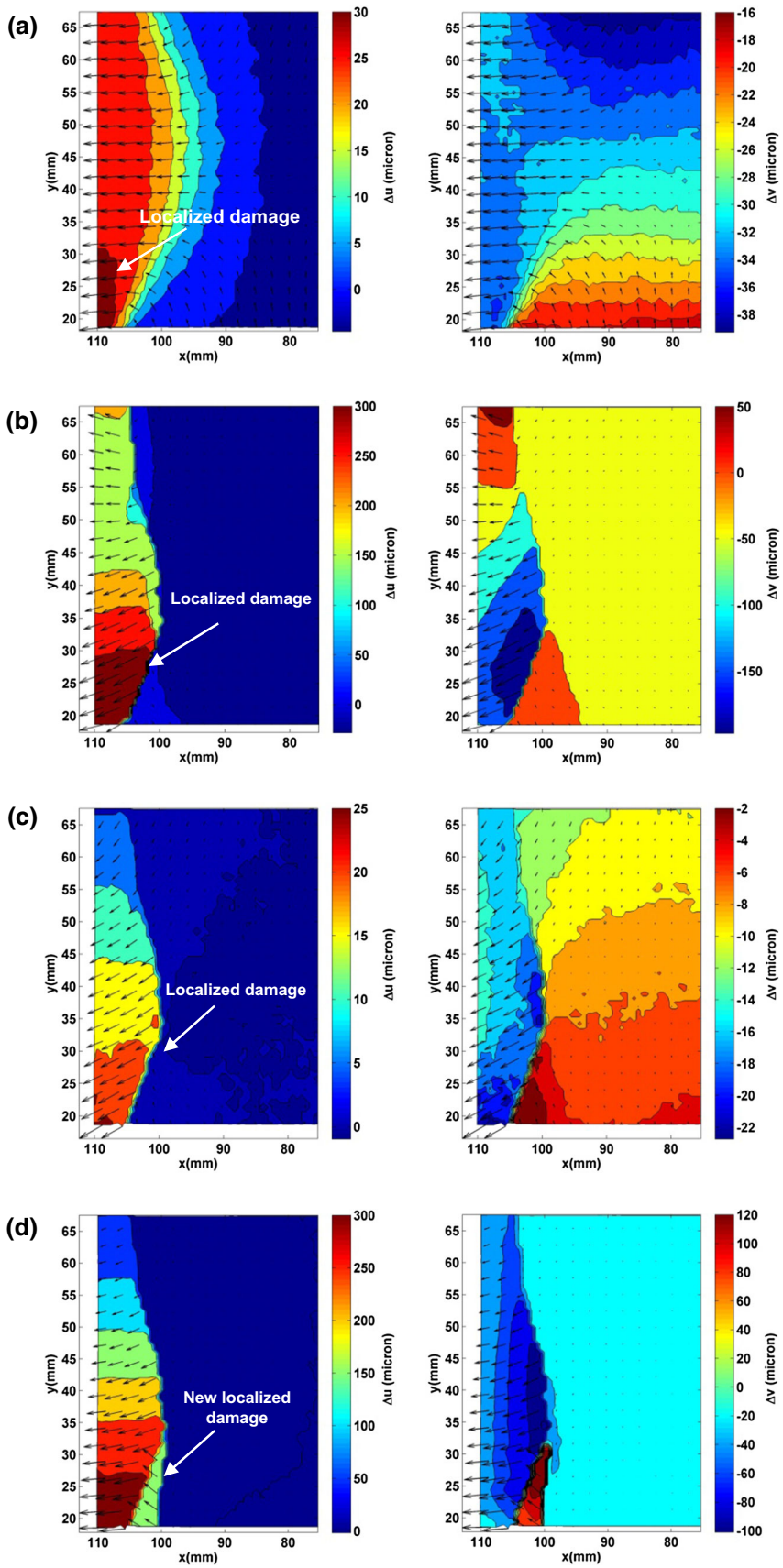

Fig. 6 Incremental horizontal (Δu) and vertical (Δv) displacement fields for test SIBS10 at LR: **a** 80–90 %; **b** 90–95 %; **c** 95–98 %; **d** 98–99 % and **e** 99–100 %

Fig. 6 continued

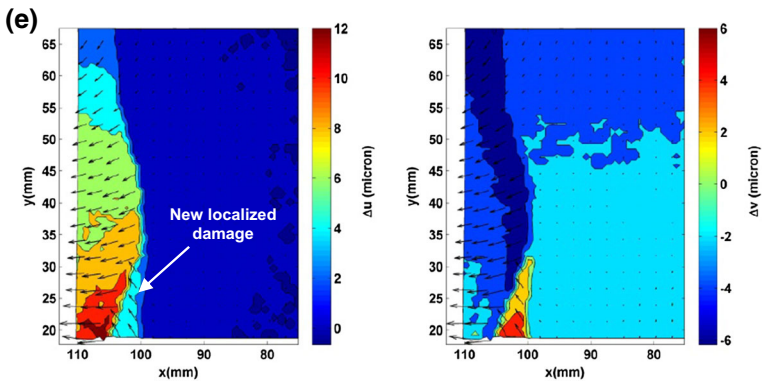

In a continuum damage model, the choice of an internal damage variable is not fixed, and it depends on the material and the user requirements. In the case of isotropic damage such as randomly orientated microcracks, a single scalar parameter represents the state of damage. The scalar parameter could be the effective area for stress transfer (Lemaitre 1985) or the crack density α (Kachanov 1986):

$$\alpha = \frac{1}{V}\sum_{i=1}^{N} A_i^{\frac{3}{2}}, \tag{1}$$

where A_i is the size of microcrack; N is the total number of microcracks; V is the total volume of the material. In addition, for materials containing spherical voids, the void density (porosity) may be suitable for the damage variable (Cowin and Nunziato 1983). Indeed, the damage field is seldom isotropic, especially when the damage level grows preferentially (e.g., uniaxial compression). A tensorial parameter can be introduced to consider the distribution of microcracks, including sizes and orientations (Kachanov 1986).

5.2 Damage Model

A phenomenological model for the surface instability test is proposed to investigate damage evolution. It is assumed that the major compressive stress is controlled by the evolution of damage associated with opening of microcracks. Using the sign convention of compression positive, a uniaxial continuum damage model can be written as (Vardoulakis and Papamichos 2000):

$$\sigma = f(\varepsilon, \Theta), \tag{2}$$

where σ and ε are axial stress and strain, respectively; Θ is Kachanov's continuity function working as an internal variable, ranging from 0 to 1, where $\Theta = 1$ means that the material has no damage. Note that damage is defined as the complementary part of the continuity Θ by

$$\Theta = 1 - D,\ 0 \le D \le 1 \tag{3}$$

From the results obtained with the surface instability apparatus, it is suggested that the mean axial stress $\langle\sigma\rangle$ across the contact area can be treated as acting on a composite material with two phases that are linked in parallel and experience the same strain; the sum of two partial stresses yields the total stress:

$$\langle\sigma\rangle = \left\langle\sigma^{(1)}\right\rangle + \left\langle\sigma^{(2)}\right\rangle \tag{4}$$

where the symbol $\langle\ \rangle$ stands for the mean value of the bracketed parameter. The stresses in the two rock phases are:

$$\left\langle\sigma^{(1)}\right\rangle = A\varepsilon \tag{5}$$

$$\left\langle\sigma^{(2)}\right\rangle = \langle\Theta\rangle B\varepsilon^3 \tag{6}$$

$$\langle\Theta\rangle = 1 - m\varepsilon^{1.5} \tag{7}$$

The exponent of 1.5 is selected based on Hertzian theory for grain-to-grain contact (Vardoulakis and Papamichos 2000). Equation (5) represents the first rock phase that features a linear elastic stress–strain relation, and this phase does not experience damage. Equation (6) represents the stress in the second rock phase, the damaged component, which captures the damage process, and its performance follows a nonlinear irreversible damage law, as described by the continuity function in Eq. (7) representing the state of the second rock phase. The damage only evolves during loading (increasing strain) and is irreversible. The average level of damage can be defined as:

$$\langle D\rangle = 1 - \langle\Theta\rangle \tag{8}$$

Figure 7 shows that no significant AE events were recorded until the loading ratio reached 30–40 %, and this observation is typically reported with different types of tests on rock (e.g., Shah and Labuz 1995). Thus, it is de-sirable to set the continuity $\langle\Theta\rangle$ to start evolving after reaching a certain level of axial strain ε_i since axial strain is the driving parameter in the damage model. We introduce

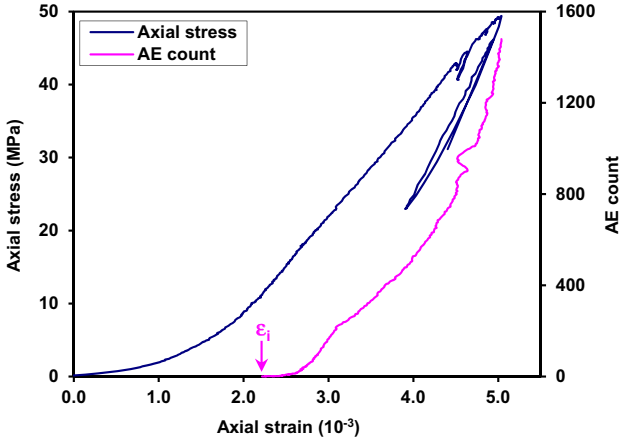

Fig. 7 Axial stress–strain curve and AE history of SIBS12. No microcracks are generated until ε_i (approximately at 30 % LR)

the damage initiation strain ε_i, such that the continuity Θ does not degrade until the applied axial strain exceeds ε_i. The original continuity function in Eq. (7) can be written as:

$$\begin{aligned} \langle \Theta \rangle &= 1 \quad \text{when } \varepsilon_{\mathrm{d}} \leq 0 \\ \langle \Theta \rangle &= 1 - m\varepsilon_{\mathrm{d}}^{1.5} \quad \text{when } \varepsilon_{\mathrm{d}} > 0 \end{aligned} \tag{9}$$

in which,

$$\varepsilon_{\mathrm{d}} = \varepsilon - \varepsilon_i. \tag{10}$$

The variable ε_{d} is called the damage evolution strain. Note that the continuity $\langle \Theta \rangle = 1$ when $\varepsilon_{\mathrm{d}} = \varepsilon - \varepsilon_i < 0$, and both rock phases remain undamaged. Based on AE data, it is suggested that the value of ε_i be determined at 30 % LR.

Figure 8 shows the model curve using Eqs. (4–10), and the fitted stress $\langle \sigma \rangle$ provides an overall good match. The

Table 2 Fitted parameters of the damage model

Test	A (GPa)	B (10^3 GPa)	m
SIBS10	1.4	680	3650
SIBS12	2.0	560	3300
SIBS14	1.9	1010	4220
SISS05	8.2	1500	3950
SISS06[a]	6.8	375	2050
SISS08	15.0	1300	3800

[a] 600 °C thermal-treated

parameters A, B, and m are summarized in Table 2. As expected, the parameters A and B, controlling the intact and damaged rock phases, respectively, are both higher for the Serena sandstone specimens due to the higher strength and modulus compared to the Berea sandstone specimens. The only exception is the thermal-treated SISS06 specimen possessing lower A, B because of increased initial damage from treatment at an elevated temperature of 600 °C. The parameter m contributes to the shape of the curve close to peak, determining the change and reversal of the curvature.

5.3 Evaluation of the Damage Parameter

The model features one scalar damage parameter representing the average damage in a specimen, so an approach using inelastic strain to determine the damage parameter is proposed. With the displacement measurements from DIC, a strain field can provide an evaluation of inelastic behavior related to damage instead of using measurements at the specimen boundaries. For compression positive, note that the lateral (normal) strain is associated with a negative sign, meaning extension of a line element.

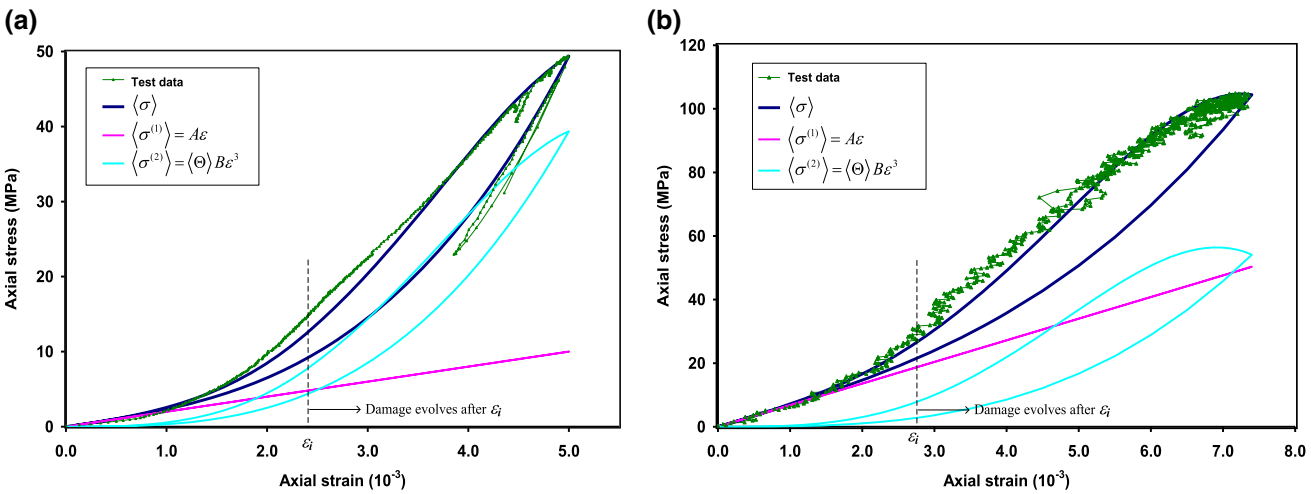

Fig. 8 Fitted stress–strain curve for test **a** SIBS12 and **b** SISS06. Continuity $\langle \Theta \rangle$ starts to degrade after the strain threshold ε_i at 30 % LR, with the undamaged component $\langle \sigma^{(1)} \rangle$ being linearly elastic

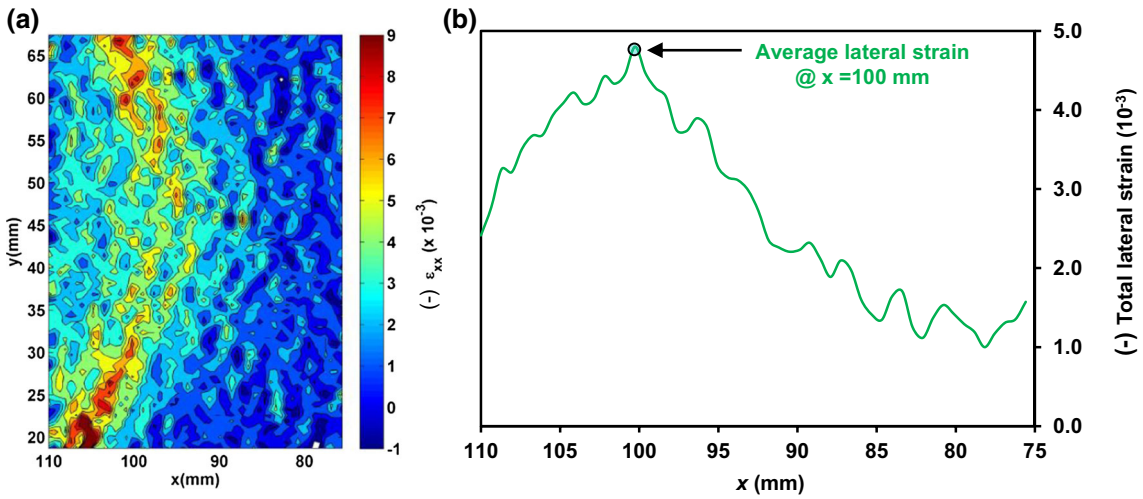

Fig. 9 **a** Total lateral strain contour at LR = 90 % for SIBS10; **b** the corresponding ε_l profile in the x-direction (average taken along y-direction)

Figure 9a shows a sample contour of the total lateral strain field (LR = 90 %, SIBS10). By taking an average along the y-direction, for example, along $x = 100$ mm, an average value is obtained (blue circle marked in Fig. 9b):

$$\varepsilon_l(x) = \bar{\varepsilon}_{xx}(x,y)|_{y=\text{const}} \tag{11}$$

A profile of ε_l in the x-direction is generated by re-peating this process (Fig. 9b).

Thus, a series of ε_l profiles are obtained at different LRs, showing the history of evolving lateral strain (Fig. 10). If the rock behaved elastically without damage, the ε_l profile would remain uniform (LR < 30 %) as axial loading is applied. It is clear that the distribution of ε_l is not uniform, where the inner part of specimen (e.g., $x < 85$ mm) displayed a lower level of lateral strain than the material close to the free surface; as LR increased, damage developed near the free surface. In fact, a higher level of lateral strain closer to the free surface starts to appear as early as 30 % LR, which matches well with the AE data, where microseismic activity was detected at similar levels of loading.

Note that total lateral strain contains both elastic and inelastic parts, as depicted in Fig. 11. According to continuum damage mechanics, the degradation of material integrity reduces the stiffness of the body. Thus, a nonlinear stress–strain behavior is associated with damage of the rock, and the observation of a non-uniform strain distribution is assumed to be due to inelastic strain related to the damage. The elastic lateral strain, ε_l^e, can be estimated using the total lateral strain averaged from the inner part ($x < 85$ mm) of the specimen by fitting a linear trend-line during initial loading (Fig. 12). Material within the inner part has minimal effects from the free face; the elastic lateral strain at higher LR is estimated by extrapolation of this trend-line. Once ε_l^e is determined for different LRs, the inelastic part of the total lateral strain $\varepsilon_l^{\text{inelastic}}$ is computed

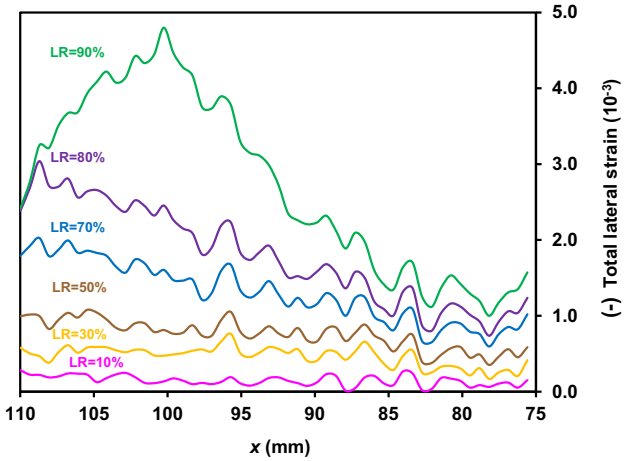

Fig. 10 History of total lateral strain ε_l profile for SIBS10

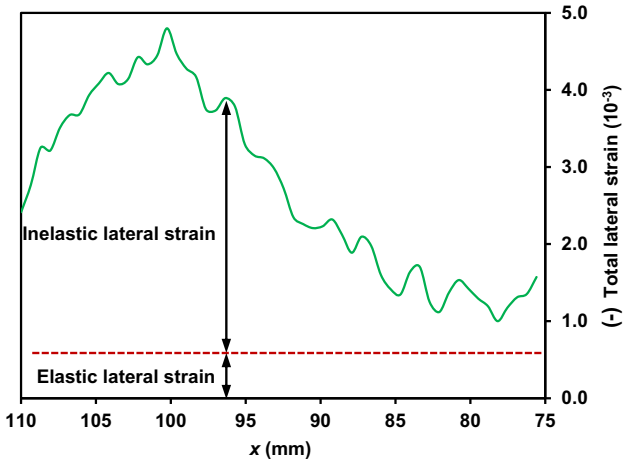

Fig. 11 Illustration of elastic and inelastic total lateral strain at 90 % LR for SIBS10

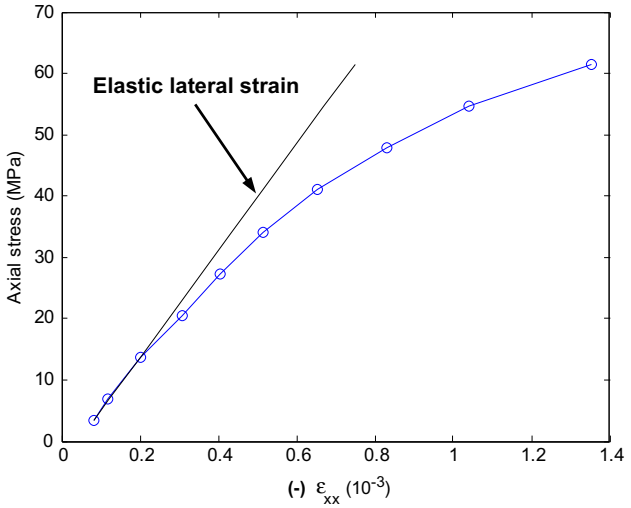

Fig. 12 Determination of elastic lateral strain (*black line*) using the lateral strain ε_{xx} within the inner portion ($x < 85$ mm) of SIBS 10

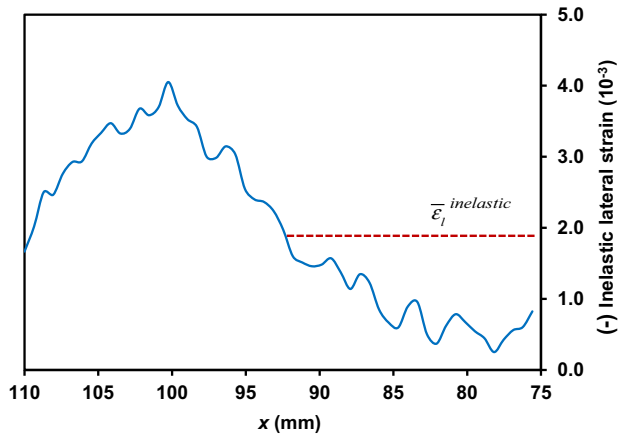

Fig. 13 Distribution of inelastic lateral strain $\bar{\varepsilon}_l^{\text{inelastic}}$ of SIBS10 at LR = 90 %, with $\bar{\varepsilon}_l^{\text{inelastic}}$ representing the average of the profile

by subtracting ε_l^e from the ε_l profile; the result is shown in Fig. 13.

The inelastic lateral strain profile is then averaged and the average inelastic lateral strain $\bar{\varepsilon}_l^{\text{inelastic}}$ is used to represent the current state of damage and it is linked to the damage parameter for each LR. To compute the average damage $\langle D \rangle$, $\bar{\varepsilon}_l^{\text{inelastic}}$ is normalized with a quantity called the damage saturation strain ε^D by

$$\langle D \rangle = \frac{\bar{\varepsilon}_l^{\text{inelastic}}}{\varepsilon^D} \tag{12}$$

The damage saturation strain ε^D is determined by matching the damage level $\langle D \rangle$ from Eq. (12) to the average damage $\langle D \rangle = 1 - \langle \Theta \rangle$ computed from the modified dam-age evolution model using Eqs. (5–10), when a fracture was visible (spalling took place). Note that the process of using

Table 3 M1odeled damage level, ε^D and $\bar{\varepsilon}_l^{\text{inelastic}}$ in surface instability tests

Test number	Modeled damage level	ε^D	$\bar{\varepsilon}_l^{\text{inelastic}}$
SIBS10	0.30	-6.8×10^{-3}	-2.0×10^{-3}
SIBS12	0.37	-5.1×10^{-3}	-1.9×10^{-3}
SISS05	0.40	-4.5×10^{-3}	-1.8×10^{-3}
SISS06	0.50	-9.0×10^{-3}	-4.4×10^{-3}

DIC images to calculate inelastic lateral strain was selected to stop at the occurrence of one or more visible fractures propagating into the field of view, i.e., surface instability in the form of spalling (localized damage) was observed. The corresponding LR was 90–95 %. For example, consider test SIBS10: the average inelastic lateral strain $\bar{\varepsilon}_l^{\text{inelastic}} = -1.97 \times 10^{-3}$; to match the modeled damage level of 0.30 at the onset of spalling, the damage saturation strain $\varepsilon^D = -6.8 \times 10^{-3}$. Table 3 summarizes the results of $\bar{\varepsilon}_l^{inelastic}$, the corresponding damage level, and ε^D for four tests, and Fig. 14 presents the history of damage evolution.

It is interesting to note that when spalling was observed, LR = 90–95 %, the average inelastic lateral strain $\bar{\varepsilon}_l^{\text{inelastic}}$ was -2.0×10^{-3} (SIBS10), -1.9×10^{-3} (SIBS12), -1.8×10^{-3} (SISS05), and -4.4×10^{-3} (SISS06). Thus, for the two Berea specimens and the virgin (i.e., no thermal treatment) Serena specimen, $\bar{\varepsilon}_l^{\text{inelastic}}$ values are fairly close. This implies that a critical value of the inelastic lateral strain for spalling $\bar{\varepsilon}_{\text{lcr}}^{\text{inelastic}} = -2.0 \times 10^{-3}$ may serve as an index for surface instability phenomenon in these two virgin sandstones.

It should be emphasized that the damage (or continuity) parameter in the model is a qualitative measure of the specimen's current state in relation to its initial one, which is assumed to have zero initial damage, i.e., $\langle \Theta \rangle = 1$. Two specimens of Serena sandstone possessed very different levels of initial damage, as SISS06 was heated to 600 °C. The purpose of the thermal treatment was to induce microcracking in the quartz-rich rock in the absence of mechanical loading. This is achieved by heating the material to reach the α–β phase transition of quartz at 573 °C, which creates significant microcracking due to an increase in volume. Biolzi et al. (2011) reported that the modulus degraded 35 % from the virgin material (12.7 GPa) to the 600 °C treated (8.2 GPa). The degradation was accompanied by an increase in pre-peak nonlinearity as a consequence of thermally induced microcracking. As reported in Table 3, when surface instability occurred, the critical inelastic lateral strain $\bar{\varepsilon}_{\text{lcr}}^{\text{inelastic}}$ was -1.8×10^{-3} for the virgin material and -4.4×10^{-3} for the 600 °C-treated rock. The thermal-treated specimen exhibited a twice-larger level of lateral inelastic strain prior to spalling, a direct result of the increase in initial damage.

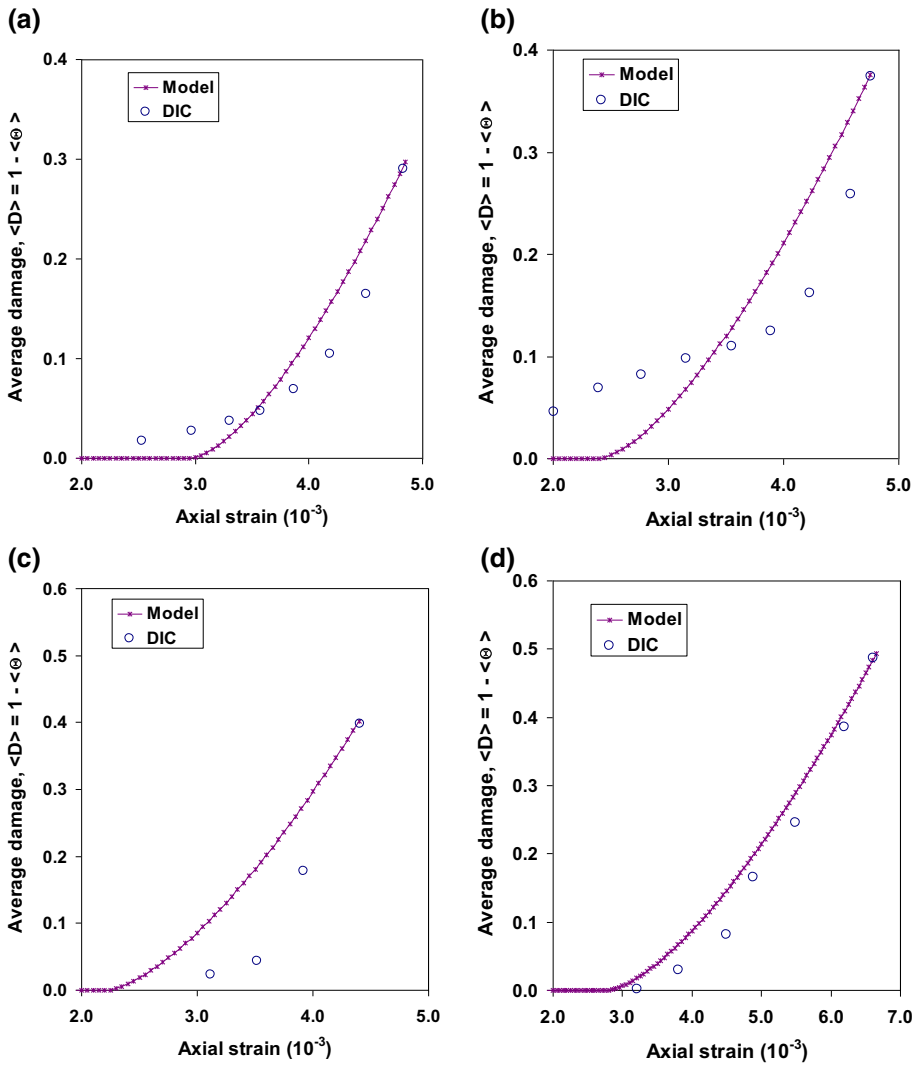

Fig. 14 Average damage evaluated for **a** SIBS10, $\varepsilon^D = -6.8 \times 10^{-3}$; **b** SIBS12, $\varepsilon^D = -5.1 \times 10^{-3}$; **c** SISS05, $\varepsilon^D = -4.5 \times 10^{-3}$; **d** SISS06, $\varepsilon^D = -9.0 \times 10^{-3}$

6 Conclusions

Acoustic emission (AE) and digital image correlation (DIC) were used to monitor and record the history of damage during the occurrence of surface spalling, which is a predominantly planar fracture phenomenon. The patented surface instability apparatus was used to replicate a plane-state of strain near the free surface in a semi-infinite medium subject to far-field compressive stress. Surface instability tests were successfully performed using specimens of Serena sandstone and Berea sandstone.

Comparing the AE locations that were determined in three dimensions to the crack trajectory mapped after the test showed a consistent pattern with the crack orientation. However, AE locations at different loading stages revealed scattered, not highly clustered patterns. Nevertheless, the AE locations at different stages imply some level of damage evolution, migrating from the free face into the interior part of the specimen.

DIC is a modern technique of pattern matching that computes the displacement field between the reference and current images taken from a solid surface before and after deformation. The axial and lateral displacement fields suggested that the displacement gradient was uniform in both directions at early loading, roughly below a load ratio, LR = current load/peak load, of 30 %. At 70–80 % LR, the free-face effect started to show in the displacement contours, especially for the lateral displacement measurements. As the axial stress increased close to peak stress, extensional lateral strain started to show concentrations associated with localized damage.

Continuum damage mechanics was used to describe damage evolution in the surface instability test. The macroscale (average) axial stress–strain relation was modeled by two phases of material linked in parallel, similar to a composite material model. The average axial stress–strain behavior was firstly fitted by the composite model to obtain the material parameters. To quantify the damage variable,

the inelastic lateral strain $\bar{\varepsilon}_l^{\text{inelastic}}$ computed from DIC information was selected as the reference of damage. By normalizing with a damage saturation strain, the history of damage was traced and compared with the modeled value, which showed reasonable consistency. The critical value of inelastic lateral strain $\bar{\varepsilon}_{\text{lcr}}^{\text{inelastic}}$ was selected at the onset of surface instability (localization) captured by the digital imaging system. The two sandstones, Serena and Berea, exhibited approximately the same value at $\bar{\varepsilon}_{\text{lcr}}^{\text{inelastic}} = -2 \times 10^{-3}$, which may provide a metric for determining the onset of surface spalling.

Acknowledgments Partial support was provided by the MSES/Miles Kersten Chair and the Research Council of Norway through project #215667, "Formation reinforcement for wellbore stability and sand control." Il Casone Group, Firenzuola (Florence) provided assistance with selection and preparation of the Serena sandstone specimens.

References

Andersson JC, Martin CD, Stille H (2009) The aspo pillar stability experiment: Part II—rock mass response to coupled excavation-induced and thermal-induced stresses. Int J Rock Mech Min Sci 46:879–895

Biolzi L, Labuz JF, Muciaccia G (2011) A problem of scaling in fracture of damaged rock. Int J Rock Mech Min Sci 48:451–457

Cowin SC, Nunziato JW (1983) Linear elastic material with voids. J Elast 13:125–147

Diederichs MS (2007) Mechanistic interpretation and practical application of damage and spalling prediction criteria for deep tunneling. Can Geotech J 44(9):1082–1116. doi:10.1139/T07-033

Ewy RT, Cook NGW (1990) Deformation and fracture around cylindrical openings in rock-I. Observations and analysis of deformations. Int J Rock Mech Min Sci Geomech Abstr 27(5):387–407

Horii H, Nemat-Nasser S (1985) Compression-induced microcrack growth in brittle solids: axial splitting and shear failure. J Geophys Res 90(B4):3105–3125

Hudson JA, Brown ET, Fairhurst C (1971) Shape of complete stress-strain curve for rock. In: Proc 13th symposium on rock mechanics, University of Illinois, Urbana, IL

Kachanov ML (1986) Introduction to continuum damage mechanics. Martinus Nijhoff Dordrecht, The Netherlands

Kachanov ML (1993) Elastic solids with many cracks and related problems. Adv Appl Mech 30:259–428

Krajcinovic D (1983) Constitutive theory of damaging materials. J Appl Mech 50:355–360

Krajcinovic D (1989) Damage mechanics. Mech Mater 5:117–197

Krech WW, Henderson FA, Hjelmstad KE (1974) A standard rock suite for rapid excavation research. Report of Investigations 7865, U.S. Bureau of Mines

Labuz JF, Bridell JM (1993) Reducing frictional constraint in compression testing through lubrication. Int J Rock Mech Min Sci Geomech Abstr 30:451–455

Lemaitre J (1985) A continuous damage mechanics model for ductile fracture. J Eng Mater-T ASME 107:83–89

Lin Q, Labuz JF (2013) Fracture of sandstone characterized by digital image correlation. Int J Rock Mech Min Sci 60:235–245

Nemat-Nasser S, Horii H (1982) Compression-induced nonplanar crack extension with application to splitting, exfoliation, and rockburst. J Geophys Res 87(B8):6805–6821

Papamichos E, Labuz JF, Vardoulakis I (1994) A surface instability detection apparatus. Rock Mech Rock Eng 27:37–56

Peng S, Johnson AM (1972) Crack growth and faulting in cylindrical specimens of Chelmsford granite. Int J Rock Mech Min Sci Geomech Abstr 9:37–86

Schapermeier E (1979) Formulierung eines Gebirgsschlagkriteriums fur den steinkohlenbergbau mit Hilfe eines Finite-Differenzen-Verfahrens (Formulation of a rockburst criterion for hard coal mining using a finite difference method, In German). Publication IBF, Issue 83, University of Karlsruhe, Karlsruhe

Shah KR, Labuz JF (1995) Damage mechanisms in stressed rock from acoustic emission. J Geophys Res 100(B8):15527–15539

Stacey TR (1981) A simple extension strain criterion for fracture of brittle rock. Int J Rock Mech Min Sci Geomech Abstr 18(6):469–474

Vardoulakis I, Papamichos E (2000) Anisotropic damage diffusion. International Symposium on Recent Advances in Mechanics. In: Honor of A.N. Kounadis. Athens, Greece

Vardoulakis I, Papanastasiou PC (1988) Bifurcation analysis of deep boreholes: I surface instabilities. Int J Numer Anal Meth Geomech 12(4):379–399

Vardoulakis I, Labuz JF, Papamichos E, Tronvoll J (1998) Continuum fracture mechanics of uniaxial compression on brittle materials. Int J Solids Struct 35:4313–4335

Wawersik WR, Fairhurst C (1970) A study of brittle rock fracture in laboratory compression experiments. Int J Rock Mech Min Sci Geomech Abstr 7(5):561–575